Helicopter Rotor Morphing for Performance Improvement in Reverse Flow Conditions

Matthew DiPalma **Richard Healy** **Etana Ferede** **Farhan Gandhi**
Center for Mobility with Vertical Lift (MOVE), Rensselaer Polytechnic Institute, Troy, New York

Zaffir Chaudhry **Andrzej Kuczek**
Raytheon Technologies Research Center
East Hartford, Connecticut

Daniel Camp
U.S. Army Combat Capabilities Development Command
Aviation & Missile Center
Fort Eustis, Virginia

ABSTRACT

The present study focuses on morphing of the inboard section of a helicopter rotor blade to improve aerodynamic performance in high-speed flight with significant reverse flow. Starting with the SC325218 airfoil, CFD simulations show that morphing only its lower surface, aft of the spar, to a modified ellipse geometry results in a significant reduction of reverse flow drag on the retreating side while limiting aerodynamic penalties in normal flow conditions on the advancing side. The study develops a morphing structure concept that transitions between the SC325218 airfoil and the derivative geometry while being able to carry aerodynamic loads. Key to this concept is the design of a morphing cellular lattice in the mid-chord region (25-65% chord), operating in collaboration with a specialized two-segment lower surface skin, and actuation ribs connected by spanwise stringers which also support aerodynamic loads in the aft-chord section. The cellular lattice's geometry is determined through optimization and the lattice is successful in morphing to the target geometry for high-speed operation. Parametric variations in lattice modulus, lower surface compliant skin modulus, and actuation strain are conducted toward minimizing actuation load and peak lattice strains, and key insight into the operational aspects of this morphing system are developed.

INTRODUCTION

VTOL aircraft operating at high speeds (200-250 knots) with edgewise rotors experience large regions of reverse flow over the inboard sections of blades on the retreating side of the rotor disk. In the reverse flow region, the rotor blade sections experience severely degraded performance characteristics, including negative lift, high drag, and large dynamic pitching moments, and vibration and control loads, all of which limit the maximum speed capability of the aircraft.

A number of different approaches have been considered to alleviate these problems. For example, in the development of their X2 technology, Sikorsky Aircraft modified the inboard region of the blade significantly by reducing the chord and pitch, and switching from conventional airfoils to elliptical airfoils [1]. Although these changes were beneficial to the reverse flow conditions experienced in high-speed flight on the retreating side of the rotor disk, they were detrimental to the performance of the rotor in hover and low-speed operation, as well as at high speeds on the advancing side.

Another approach considered was quasi-statically introducing reflex camber over the inboard sections of the rotor blade in high-speed flight to reduce reverse flow drag [2, 3]. While this method was effective in improving reverse flow aerodynamics, in the absence of 1/rev actuation it led to significant lift and drag penalties on the advancing side of the rotor disk [3].

The present study focuses on exploring quasi-static geometry change over the inboard section of the rotor blade in high-speed flight to improve reverse flow aerodynamics, while minimizing any associated performance losses on the advancing side. High fidelity computational fluid dynamics (CFD) simulations are executed to compare various candidate airfoil geometries and their aerodynamic performance in both normal and reverse flow conditions (corresponding to the advancing and retreated sides of the rotor disk in high-speed operation). After identifying target airfoil shapes for high-speed operation, the study focuses on the design and analysis of a morphing structure that in conjunction with an appropriate skin and actuation system can transition the inboard section of the blade between low-speed and high-speed geometries, while being able to carry the aerodynamic loads.

AERODYNAMIC MOTIVATION

The 18% thick SC325218 airfoil is used as the baseline airfoil in this study. The SC325218 (at ~40% span on the Sikorsky X2 high-speed coaxial helicopter) has a rounded leading-edge and a sharp trailing-edge, and notionally a conventional airfoil similar to it could be extended all the way inboard. While it

Presented at the Vertical Flight Society's 76th Annual Forum & Technology Display, Virginia Beach, VA, October 6-8, 2020.

could be expected to perform well in hover and low-speed operating conditions, and on the advancing side in high-speed conditions, it would perform poorly on the retreating side in high-speed conditions (where it would experience reverse flow). On the other hand, several studies (e.g., Refs. 4, 5) have shown that elliptical airfoils perform reasonably well under reverse flow conditions, so the present study first considered morphing the aft section of the SC325218 airfoil (30% chord to the trailing-edge) to an ***ellipse*** in high-speed operating conditions (see Fig. 1). As seen in Fig. 1, the SC325218 airfoil's thickness at 30% chord corresponds to the minor axis of the ellipse, and 70% of its chord length corresponds to the semi-major axis of the ellipse. However, this modification leads to a blunt trailing-edge, and recognizing the challenge associated with morphing from a sharp trailing-edge (on the classical SC325218) to a completely blunt trailing-edge, a ***modified ellipse*** (also shown in Fig. 1) is additionally considered. This second geometry departs from that of the ellipse over the section extending from 70% chord to trailing-edge. The shape, over this last 30% chord region, is defined by a cubic spline with slope continuity with the ellipse at 70% chord and a ±30° angle with the chord line at the trailing-edge. Finally, a third geometry (referred to as ***lower surface modified ellipse***) is considered where the top surface of the SC325218 airfoil is left unchanged, and only the bottom surface (extending from 30% chord to the trailing-edge) morphs to the modified ellipse geometry in high-speed flight. Figure 2 shows a close-up of the four geometries in the trailing-edge region.

The aerodynamic analysis uses the commercial Navier-Stokes solver, AcuSolve, previously used in rotorcraft problems at Rensselaer Polytechnic Institute in Refs. 6-10. AcuSolve CFD simulation results of the aerodynamic characteristics of the baseline SC325218 and the three morphed geometries are shown in Figs. 3-5. Figures 3 and 4 show the airfoil lift and drag coefficients versus angle of attack in normal flow (flow going from the rounded nose toward the trailing-edge). These simulations are carried out at a Mach number of 0.5, broadly representative of inboard sections on the advancing side in high-speed flight (200-250kts). Figure 5 shows the airfoil drag coefficient in reverse flow (flow going from the trailing-edge toward the rounded nose). These simulations are carried out at a lower Mach number of 0.25, corresponding to conditions on the retreating side.

In Fig. 3, the ellipse and its derivative geometries all have a lower (but comparable) lift coefficient in normal flow than the SC325218. But since there is plenty of lift available on the advancing side due to high dynamic pressure this reduction in lift is not hugely problematic. More significantly, Fig. 4 indicates that the drag on the advancing side is very large for the ellipse and the modified ellipse, but the lower surface modified ellipse has a drag that is generally comparable to that of the baseline SC325218.

From Fig. 5 it is observed that the baseline SC325218 generates the highest drag in reverse flow (at a 6° reverse flow angle of attack the Cd value is 5x greater than at 6° in forward flow seen in Fig. 4). While the ellipse has the lowest drag in reverse flow its derivative geometries perform almost as well at low to moderate angles of attack. At 6° angle of attack in reverse flow, Fig. 5 shows that the drag for the modified ellipse and lower surface modified ellipse is around 36% higher than the ellipse, while the SC325218 is 137% higher.

Figure 6 shows the flow field around the four airfoils discussed in this section at a 6° reverse flow angle of attack. All airfoils display a bluff body separation in the vicinity of the rounded nose, that is a source of drag, but the SC325218 also shows a significant separation region on the lower surface that is an additional significant source of drag. The ellipse, modified ellipse, and lower surface modified ellipse do not show lower surface separation, and this contributes to the reduced drag in reverse flow (seen on Fig. 5).

Based on the CFD simulation results, the SC325218 with lower surface modified ellipse is selected as the target geometry for high-speed flight. Figure 7 shows the two geometries overlaid, the SC325218 for low and moderate speed operation, and the SC325218 with lower surface modified ellipse for high-speed operation where reverse flow conditions are dominant. The selection of the SC325218 with lower surface modified ellipse for high-speed operation is made on the basis that it provides the lowest drag under normal flow conditions and a relatively low level drag at moderate angles in reverse flow. Due to the upper surface being unchanged from the baseline SC325218, morphing to this geometry would also be much easier to implement (and actuate). The lift coefficients for the four geometries in reverse flow are not a major consideration in the selection of the high-speed geometry.

The following sections of this paper focus on the design of a morphing structure, which in conjunction with an appropriate actuation system and lower-surface skin can transition between the geometries shown in Fig. 7, while being able to carry the aerodynamic loads. For reference, the aerodynamic pressures acting on the lower surface of the airfoil at 9° angle of attack (from AcuSolve) are shown in Figure 8. The advancing side pressures are calculated at Mach 0.5 and the retreating side pressures at Mach 0.25, with a x4 factor of safety, in both cases. In reverse flow, the entire lower surface is under moderate suction loads, while under normal flow, the leading edge is under pressure and the trailing edge experiences suction.

MORPHING STRUCTURE CONCEPT

Figures 9a-9c show a high level schematic representation of the overall structural design and actuation strategy in the inboard morphing section of the blade. The figure shows kinematic actuation linkages (in grey) at selected spanwise stations, essentially acting as morphing ribs. These span-wise spaced linkages are driven by a single rotary actuator at the root end. The actuation linkage connects directly to the lower skin at three points at 53%, 68%, and 85% chord, and prescribes motion at these locations (ensuring these points

move precisely to the lower surface modified ellipse contour). The lower surface skin (in yellow) has two sections, a shorter length, softer in-plane compliant section from 25% to approximately 45% chord, which accommodates all in-plane strains; and from 45% chord, a stiffer composite section to the trailing edge. Together, they carry the aerodynamic loads as well as accommodate the in-plane and bending strains due to morphing, while providing requisite bending stiffness in chordwise and spanwise directions

Shown in orange in the spanwise sections between the morphing ribs is a tailored cellular lattice core extending from 25% chord (aft of the spar) to 65% chord. The cellular lattice core is designed to enable/ assist the desired shape-change while carrying aerodynamic pressure. Also seen on the figure are three rigid spanwise stringers (in black) connecting between the actuation linkages at 53%, 68%, and 85% chord. These stringers provide primary support to the skin against aerodynamic loads in the aft-chord sections (where no cellular lattice is present), while adding to the support provided by the cellular lattice core in the mid-chord section. The stringers also impose a spanwise constancy and allow the morphing structure analysis to be carried out at a two-dimensional cross-sectional level.

STRUCTURAL DESIGN AND ANALYSIS OF MORPHING CELLULAR LATTICE

In order to design a structure that can morph from the baseline SC325218 airfoil to the target geometry (SC325218 with lower surface modified ellipse), and back, a specialized cellular lattice core is implemented. Cellular lattice structures have been previously used for morphing applications [11-15] and offer a high degree of design flexibility. In the present study a morphing cellular lattice is introduced in the region aft of the leading-edge spar, as shown in Fig. 10. The lattice, which spans from 25-65% chord is comprised of hexagonal cells that are auxetic, which means that they exhibit a negative Poisson's ratio. As a result, extending the lattice in the chordwise direction (toward the trailing-edge of the airfoil) would result in an increase lattice thickness, which in turn induces an increase in airfoil thickness, compatible with the shape change desired to meet the target high-speed geometry.

Design Variables

The cellular lattice in the region aft of the leading-edge spar has identical rows of cells, but the cell geometry varies over twelve columns of cells. The twelve columns of cells provide a sufficiently dense skin support, and further reduction in cell size (with associated increase in numbers of rows and columns of cells along with thinner cell walls) would only increase manufacturing complexity. The corners of the lattice grid (horizontally hatched region in Fig. 10) define the space allotted to each individual cell in the lattice. Within these boundaries, an individual unit cell (as shown in Fig. 11) can be uniquely characterized by two parameters. First, the hourglass ratio, h, defines the ratio of the vertical wall height to the distance between the vertices marked A and B in Fig. 11. This parameter controls the effective maximum Poisson's ratio of the cell. A cell with an hourglass ratio of 2 could, if completely stretched, double the vertical distance between points A and B. As depicted in Fig. 12, an hourglass ratio of 1 would therefore correspond to a rectangular cell, while an hourglass ratio of 6 would correspond to a cell which is tightly pinched in the center. Second, the wall thickness ratio, β, represents the ratio of the wall thickness to the length of the inclined wall. This parameter governs the slenderness ratio of the cell walls in the lattice, which controls the relative stiffness between cells. Because the vertices of the unit cells are not defined by a strictly rectangular grid, the cells are not necessarily symmetric across any axis.

As shown in Fig. 13, the auxetic lattice is connected to a rigid upper support by a series of twelve stumps. Similarly, it connects to the lower skin by a series of twelve stumps. The thicknesses of these stumps are defined in the same manner as the wall thickness, β: β_U represents the thickness of the upper stump relative to its length and β_L represents the thickness of the lower stump relative to its length. Moving in the aft-chord direction, Fig. 13 shows the stumps provided with a progressively increasing tilt. On application of an actuation strain, the goal is for these stumps to straighten out and assist with thickness change (effectively increasing the negative Poisson's ratio of the auxetic lattice). On the other hand, beginning with straight stumps would lead to them undergoing large rotations during lattice chordwise actuation, detracting from desired thickness change. The tilt of the stumps is related to the applied lattice strain, and is not one of the design variables.

In this study, each of the twelve columns of lattice cells along the chord of the airfoil has a varying upper stump thickness, β_U, lower stump thickness, β_L, cell wall thickness, β, and hourglass ratio, h. Note that β and h do not vary from row-to-row. Thus, a total of 48 independent variables are considered in the design of the cellular lattice core.

Structural Analysis

The embedded lattice structure is analyzed using the commercial finite element analysis software ABAQUS version 6.13. The full structural model is presented in Fig. 14 An airfoil chord length of 0.5 meters (19.6") is considered for the analysis.

The lattice is constrained at the rigid spar, and its upper vertical stumps are connected to the rigid upper blade structure, which is essentially an extension of the leading edge D-spar. The lower lattice stumps are connected to a two-segment blade skin. The skin from extending from 25-45% chord is relatively compliant in-plane, while the skin extending aft of 45% chord is relatively stiff. The flexible and stiff sections of the skin were modeled using the material properties presented in Table 1. The right end of the lattice is extended by 4% of the lattice length in the chordwise direction.

The skin attached to the lower surface of the lattice has a constant thickness of 0.3265% chord (0.064"). The aft chord section is supported and actuated by two spanwise stringers at 68% and 85% chord which apply the precise amount of displacement required to move the skin into the desired lower surface shape. The third stringer, depicted at 53% chord in Figures 9a and 9b was not included in the model for the optimization because the objective was to have the cellular lattice itself produce the desired profile change in the mid-chord sections, without the assistance of the stringer. The stringer at 53% chord is available as an additional resource to fine-tune the lower surface profile, if necessary. The skin is also hinged at the trailing edge to accommodate the significant change in local curvature required by the actuation process.

The cellular lattice system was modeled and analyzed under forward and reverse flow aerodynamic pressures (shown in Fig. 8) using a lattice modulus of 500 MPa which was determined to be more than sufficient to carry aerodynamic pressure loads. Further increase in lattice stiffness would unnecessarily increase actuation force requirement and system weight, with no added structural benefit.

Table 1. Lattice and Skin Material Properties

Structure	Elastic Modulus (E)	Poisson's Ratio (ν)
Lattice Core	500 MPa	0.3
Flex Skin	3.0 GPa	0.48
Stiff Skin	63.4 GPa	0.3

The entire system is modeled using two-dimensional shell elements with around 100,000 linear elements in total. This corresponds to an average element size that is around 20% of the lattice cell wall thickness as shown in Fig. 15, which has been previously shown to give mesh-converged results for shell analysis of cellular lattice structures (Ref. 16).

Optimization Procedure

The optimization was carried out using MATLAB's built-in 'active-set' algorithm for the 'fmincon' routine. The 48 design variables for the lattice were optimized such that the lower surface would approach the target geometry in Fig. 7 (with minimum integrated RMS error over the mid-chord section) under actuation (4% chordwise strain at the right end of the lattice) and aerodynamic loads previously described. The design variables are:

$$X = [\beta^1, \dots, \beta^{12}, \beta_U^1, \dots, \beta_U^{12}, \beta_L^1, \dots, \beta_L^{12}, h^1, \dots, h^{12}]'$$

Of the design variables, the lattice cell wall thicknesses and stump thicknesses were constrained to remain between 4-10% of the local inclined cell wall length (fairly typical in cellular lattice structures) and the hourglass ratio was permitted to vary between 1-6. The initial guess for the optimization was set at the midpoint between the limits on the design variables.

The peak strains in the structure were closely monitored during the optimization process, but were not imposed as a constraint. As a result of the boundary conditions, the peak strain always occurred within the cell at the upper-right corner of the lattice. The peak strain was only moderately sensitive to the single upper-rightmost vertical stub thickness. A sensitivity study is presented in a following section to discuss the impact of relevant model parameters on lattice peak strains.

The position of the lower airfoil skin was monitored at the 12 chordwise locations corresponding to the attachment points between the lower lattice stubs and the lower airfoil skin, between 25-65% chord. The deformation at chordwise locations aft of 65% is not considered in the optimization because displacements are explicitly enforced in the aft-chord section at 68% and 85% chord by the kinematic actuation mechanism and rigid stringers. Simulation results show that this enforcement, along with the stiff aft-skin is sufficient to meet the target profile, and to hold the shape under aerodynamic loading. As part of each iteration of optimization procedure, for successive updates to the design, the structural analysis evaluates the vertical distance between points on the lower skin that the lattice stumps connect to (y_i) and the desired position of those points (based on the target lower surface profile). The formal objective of the optimization was:

$$minimize \quad g(X) = \frac{1}{24}\sqrt{\sum_{i=1}^{12}(y_i^{NF} - y_i^*)^2 + \sum_{i=1}^{12}(y_i^{RF} - y_i^*)^2}$$

$$subject\ to \quad 1 \le h^i \le 6$$

$$0.04 \le \beta^i, \beta_U^i, \beta_L^i, \le 0.10$$

Where the superscript *NF* refers to aerodynamic loading under normal flow (representative of the advancing side), *RF* refers to aerodynamic loading in reverse flow (representative of the retreating side), and the superscript *(-)** refers to the target geometry.

Results

The optimized design variables are plotted in Figs. 16a and 16b. The cell wall thickness varies from 7.6% near the spar, decreasing to a minimum value of 6.0%, and increases to 7.0% at 65% chord. The upper stub thicknesses range from 5.0-7.1%, and the lower stub thicknesses range from 4.1-7.0%. The hourglass ratio, h, increases from 1.1 at the spar to 1.6 at 65% chord. While the small variations in the wall thickness values are likely just manifestations of the optimizer fine-tuning the design variables to minimize the error in the objective function, the overall hourglass ratio distribution is

the dominant contributor to the objective, and facilitates the overall shape change.

As shown in Fig. 17, the post-actuation lower skin profile (yellow) closely matches the target profile (in red) for the optimized design. Also seen in yellow is the deformed lattice, while the original lattice boundaries and SC325218's lower surface profile are shown in black. The RMS error between the lower skin and the target profile over the mid-chord section under lattice actuation only is 0.26% chord (an average 0.051 in deviation for an airfoil that has a 19.685 in chord and a 3.5433 in maximum thickness). The lower skin profile under reverse flow aerodynamic loads (shown in Fig. 17) has an RMS error of 0.75% chord (an average of 0.1476 in) from the target profile. These low values indicate that the optimization process was largely successful in determining a lattice structure design that could morph to the target lower surface modified ellipse geometry for high-speed conditions.

Figure 18 illustrates the lower vertical stumps in the unactuated and actuated configurations. While they are progressively tilted in the baseline SC325218 configuration, the chordwise extension of the lattice causes them to straighten out vertically in the morphed configuration. In this way, the vertical stumps, when actuated, positively contribute to the thickness change of the lattice structure. On the other hand, had the vertical stumps been vertical in the base configuration, their subsequent actuation strain induced tilt would have detracted from the thickness change delivered by the lattice.

An evaluation of the lattice strains for the morphed configuration indicated that the highest strains occurred in the upper right corner. Figure 19 shows the deformed corner cell and a peak strain close to 20% is observed. Although the strains are shown under combined loading (applied morphing strain and reverse flow aerodynamic loads on the morphed lower surface), the applied morphing strain is by far the dominant contributor. The peak strain at the top right is due to combination of the effects of the fixed upper boundary and the highest deformations in the last column of cells because they have the highest hourglass ratio. Other cells in this column, away from the fixed upper boundary effect, have peak strains under 12%. While the maximum lattice strains are an important factor in lattice material selection, it may be possible to tailor/redesign the cell junctions and stumps to reduce strain peaks. Other means of reducing peak strains are also possible (and discussed in a later section).

Lower skin strains are shown in Fig. 20. The chordwise strains within the compliant skin section (from 25%-45% chord) are 1.1%, while the strains within the stiff aft skin section are substantially lower (around 0.1% over most of the stiff skin). However, a local peak of around 0.2% strain is observed in the stiff aft-skin in the vicinity of the aft-most stringer (at 85% chord) due to the local bending it induces.

DISCUSSION ON LOWER SURFACE SKIN

Figure 21 shows the notional chordwise strain distribution in the lower surface skin from 25% chord to the trailing-edge if points on the lower surface of the SC325218 (at any given spanwise station) were simply moved vertically downward to the target lower surface modified ellipse profile. The high strains at the trailing-edge are associated with high curvature change in that region and can be alleviated by using a hinged condition at the trailing-edge (not implemented on Fig. 21). More importantly, a large section of the lower skin is observed to experience strains between 0.4% and 0.8%. These strains, at any cross-section, are due to a net contour length increase associated with transitioning from the lower surface of the baseline SC325218 to the modified ellipse profile. Thus the lower skin must have the ability to undergo the requisite length change. Another issue to consider is the ability of the skin to carry aerodynamic loads, and the underlying support available. The morphing lattice structure in the mid-span section can provide good support for the skin, but introducing such a lattice in the trailing-edge region (where the required thickness change is greater and the space is less) would be a significant challenge. On the other hand, the spanwise stringers at 68% and 85% chord would be able to provide some support to the skin in the aft-chord regions.

In the absence of a lattice core in the aft-chord section, a relatively rigid (nominally 70 GPa modulus) skin is used in that region. This skin section is not expected to undergo significant extensional strain. Its low thickness, however, allows it to undergo chordwise bending to accommodate the geometry change between the lower surface of the SC325218 and the modified ellipse profile. The stringers provide the support to carry the aerodynamic pressure in the trailing-edge region. The rigid skin extends from the trailing edge all the way to 45% chord, where it connects to a compliant (nominally 3GPa modulus) skin. The compliant skin covers the 25% to 45% chord section, and with its lower modulus (in the elastomer range) would be capable of carrying the extensional strains associated with contour length increase. The support provided by the underlying lattice enables this compliant skin section to satisfactorily carry aerodynamic loads.

In summary, while Fig. 21 suggested that the skin would be required to accommodate the largest strains in the aft-chord sections, and much smaller strains in the mid-chord sections, a compliant skin was introduced in the mid-chord section (based on the availability of lattice support in this region) to work in conjunction with a stiffer skin that allows bending but little extension in the aft section (from 45% chord to the trailing-edge).

ACTUATION EFFORT AND PARAMETER SENSITIVITY

While the optimized cellular lattice was effective in producing the desired airfoil lower surface profile under an applied chordwise strain, calculation showed a relatively high

actuation force requirement (158 lbf to morph a 6 in spanwise section) and peak lattice strain (around 20%). This can be attributed in part to the objective function definition which minimized only the error between the airfoil lower surface profile and the target profile without any consideration of actuation effort or lattice strain. The present section considers variation in lattice modulus, applied chordwise strain, and compliant skin modulus and their effect on actuation effort, achieved lower surface deformation, and peak lattice strains. However, the lattice geometry (wall thicknesses, upper and lower stump thicknesses, and hourglass ratios) are held at those presented in Figs. 16 (except in the very last paragraph of this section).

Figure 22 shows the lattice deformation and lower skin profile corresponding to three lattice modulus values, 500 MPa (the nominal value used in optimization), 250 MPa and 100 MPa. Recall, that the lattice modulus was held at 500 MPa and not used as a design variable in the optimization process The deformations shown in Fig. 22 are in the presence of reverse flow aerodynamic loads. For all cases, the lower skin profile closely approximates the target profile (in red). Peak lattice strains (not shown) are similar, as well. Figure 23 shows lattice actuation force requirement versus lattice modulus, and a significant reduction in actuation effort is possible through the use of a more compliant lattice material. For example, reducing the lattice modulus from 500 MPa to 250 MPa reduces the actuation force requirement from 158 lbf to 80.5 lbf over a 6 in spanwise section. Reducing the lattice modulus to 100 MPa further reduces actuation force to 33 lbf. The ability of unactuated lattices of different moduli to carry aerodynamic pressure loads in low-speed conditions is examined in the Appendix.

While optimization was conducted with a prescribed lattice actuation strain of 4%, Fig. 24 shows the morphed configuration for applied lattice strains between 3% and 5% (and under reverse flow aerodynamic loads). A greater chordwise strain applied to the auxetic lattice would intuitively be expected to produce a larger thickness change, but interestingly, all three applied strain levels in Fig. 24 reach the target lower surface profile (in red) almost as well (this is verified by examining the RMS errors for all cases). A number of factors seem to be contributing to this. First, as the applied strain is increased, the upper and lower stumps of the last 3-4 columns (closest to the free end) show increasing rotation (starting from a nearly vertical orientation at 3% lattice actuation strain). The rotation of these stumps negates the natural tendency of the auxetic lattice to increase thickness as it is extended in the chordwise direction. Second, the cells near the right end of the lattice (which had an undeformed hourglass ratio approaching 1.6, see Fig. 16b) appear brick-like in the deformed state (hourglass ratio of nearly 1). In this configuration, these cells lose their ability to provide further thickness change under chordwise loading. And finally, the stiff skin below the right half of the lattice, which is constrained at the stingers (at 68% and 85% chord) also prevents the lattice from pushing the lower surface too far from the target profile. Figure 25 shows the required actuation force and versus applied lattice strain (for the baseline lattice modulus of 500 MPa). Reducing actuation strain from 4% to 3% lattice strain (1.6% chord to 1.2% chord, since the lattice is 40% of the chord length) results in the actuation force reducing from 158 lbf to 87.3 lbf (a 45% reduction). Figure 26 shows the peak lattice strains versus applied actuation strain. A reduction in applied strain from 4% to 3% results in a corresponding reduction in peak strain from 20% to around 14%. Clearly, a reduction in applied strain to the lattice would produce benefits in both lower actuation force requirements and lower peak strains, without compromising on the ability to meet the target lower surface profile.

Next, variation in the compliant skin modulus is considered. Like the lattice modulus, the compliant skin modulus was not a design variable in the optimization process and its value was held at 3 GPa. Figure 27 shows lattice actuation force requirement versus compliant skin modulus. Unlike the lattice modulus, reduction in compliant skin modulus does not result in a significant reduction in actuation force. This indicates that more energy is expended in deforming the lattice than in stretching the compliant skin. The peak lattice strains (not shown) are similarly insensitive to compliant skin modulus. Figure 28 shows deformation under reverse flow aerodynamic loads for a compliant skin modulus of 100 MPa (one thirtieth of the nominal 3 GPa modulus used in the rest of this study). At such a low modulus value, a slight suction induced bulging is observed between 25% to 45% chord (the region over which the compliant skin extends). Since there is little actuation benefit to reducing the compliant skin modulus to such low values, it is recommended that the modulus be at the very least in the 250 MPa to 500 MPa range (for the 0.064 in thickness considered).

Since reductions in lattice modulus and actuation strain on the lattice each resulted in reduction in actuation force requirement, a combination of the two was considered, as well. A 250 MPa lattice with 3% applied strain required only 44.6 lbf, and a 100 MPa lattice with 3% applied strain required only 19 lbf, over 6 in spanwise sections. The results are summarized in Table 3.

Table 2: Actuation force with variation in lattice modulus and applied strain

		Lattice Modulus		
		500 MPa	250MPa	100MPa
Applied Strain	4%	158 lbf	80.5 lbf (-49%)	33 lbf (-79%)
	3%	87.3 lbf (-45%)	44.6 lbf (-72%)	19 lbf (-88%)

Finally, the importance of variation in lattice properties along the chord was examined. While the variation in hourglass ratio in Fig. 16b is very important to the lattice's deformed shape under applied chordwise strain, and its ability to reach the target lower surface profile, the variation in wall thickness ratios in Fig. 16a merits closer consideration. It should be noted that, for the most part, the optimum wall thickness ratios lie between 5-7%. While the precise chordwise

variations in Fig. 16a produce a numerically optimum result, a simulation was undertaken to examine the deviation from the target lower surface profile when the wall thickness ratios were invariant along the chord. Using the mean values β= 0.066, β_U=0.058 and β_L, = 0.056, the RMS errors between the deformed lower surface profile and the target profile were found to be only 0.7% greater under actuation alone, and only 1.3% greater under actuation and reverse flow aerodynamic loads, relative to those observed with the optimal β, β_U, and β_L distributions in Fig. 16a. This indicates that using a uniform wall thickness in the right range may be sufficient as opposed to a very precise chordwise distribution. This could potentially simplify manufacturing.

CONCLUSIONS

Starting with the SC325218 (an 18% thick classical airfoil with a rounded leading edge, camber, and a sharp trailing-edge) as a point of departure airfoil for use on inboard sections of a helicopter rotor blade, CFD simulations were carried out to identify derivative geometries that would perform well in high-speed flight conditions with significant reverse flow. It was determined that morphing only the airfoil's lower surface, aft of the spar, to a modified ellipse geometry resulted in a significant reduction of reverse flow drag on the retreating side while limiting aerodynamic penalties in normal flow conditions on the advancing side.

The study then focused on the development of a morphing structure concept that allows back-and-forth transition from the baseline SC325218 airfoil (for low-speed operation) to the derivative geometry (for high-speed operation) while being able to carry the aerodynamic loads. Key to this concept was the design of a morphing cellular lattice core in the mid-chord region (25-65% chord), which when extended in the chord-wise direction, results in deformation to the target lower surface modified ellipse geometry while supporting aero-dynamic loads. The cellular lattice operates in collaboration with a specialized two-segment lower surface skin, and actuation ribs connected by spanwise stringers which also support aerodynamic loads in the aft-chord section.

The cellular lattice's geometry varies along the chord, and its design was determined using a gradient-based optimization procedure. The optimized lattice was successful in morphing to the target geometry for high-speed operation while demonstrating the ability to carry aerodynamic loads in the different representative conditions examined. Parametric variations in lattice modulus, lower surface compliant skin modulus, and actuation strain were conducted toward minimizing actuation load and peak lattice strains. A careful examination of the optimization results and the parametric variations conducted in this study offer good physical insight into the operational mechanisms of this morphing system and methods to improve the design.

ACKNOWLEDGMENTS

This research was partially funded by the US Government under Agreement No. W911W6-18-2-0005.

REFERENCES

1. Bagai, A., "Aerodynamic Design of the X2 Technology Demonstrator Main Rotor Blade," 64th Annual Forum of the American Helicopter Society, Montreal, Canada, April 2008.
2. Jacobellis, G., Gandhi, F., Rice, T., Amitay, M., "Computational and Experimental Investigation of Camber Morphing Airfoils for Reverse Flow Drag Reduction on High-Speed Rotorcraft," Journal of the American Helicopter Society, Volume 65, January 2020. https://doi.org/10.4050/JAHS.65.012001.
3. Jacobellis, G., "Improvement of High-Speed Coaxial Rotor Performance using Redundant Controls and Camber Morphing," doctoral dissertation in Aerospace Engineering, Rensselaer Polytechnic Institute, Dec 2018.
4. Lind, A. H., Lefebvre, J. N., and Jones, A. R., "Experimental Investigation of Reverse Flow Over Sharp and Blunt Trailing Edge Airfoils," 31st AIAA Applied Aerodynamics Conference, 2013.
5. Lind, A. H., Lefebvre, J. N., and Jones, A. R., "Time-Averaged Aerodynamics of Sharp and Blunt Trailing-Edge Static Airfoils in Reverse Flow," AIAA Journal, Vol. 52, (12), December 2014, pp. 2751–2764. doi: 10.2514/1.J052967.
6. Misiorowski, M., Gandhi, F., and Oberai, A., "Computational Study of Diffuser Length on Ducted Rotor Performance in Edgewise Flight," AIAA Journal, Vol. 57, No. 2, Feb 2019, pp. 796–808. https://doi.org/10.2514/1.J057228.
7. Misiorowski, M., Gandhi, F., and Oberai, A., "Computational Study on Rotor Interactional Effects for a Quadcopter in Edgewise Flight," AIAA Journal, published online August 26, 2019. https://doi.org/10.2514/1.J058369.
8. Misiorowski, Gandhi, F., and Oberai, A., "Computational Analysis and Flow Physics of a Ducted Rotor in Edgewise Flight," J. of the American Helicopter Society, available online September 16, 2019. https://doi.org/10.4050/JAHS.64.042004.
9. Healy, R., Misiorowski, M., and Gandhi, F., "A Systematic CFD-Based Examination of Rotor-Rotor Separation Effects on Interactional Aerodynamics for Large eVTOL Aircraft," *Proceedings of the Vertical Flight Society 75th Annual Forum and Technology Display*, Philadelphia, Pennsylvania, May 13–16, 2019.
10. Healy, R., Gandhi, F., Mistry, M., and Duffy, M., "A Computational Investigation of Multi-Rotor Interactional Aerodynamics with Hub Lateral and Longitudinal Canting," *Vertical Flight Society's 76th Annual Forum and Technology Display*, 2020.
11. Olympio, K. R., and Gandhi, F., "Flexible Skins for Morphing Aircraft using Cellular Honeycomb Cores," Journal of Intelligent Material Systems and Structures,

Vol. 21 (17), November 2010, pp. 1719-1735, doi:10.1177/1045389X09350331.
12. Olympio, K. R., and Gandhi, F., "Zero-Poisson's Ratio Cellular Honeycombs for Flexskins Undergoing One-Dimensional Morphing," Journal of Intelligent Material Systems and Structures, Vol. 21 (17), November 2010, pp. 1737-1753, doi:10.1177/1045389X09355664.
13. Olympio, K. R., Gandhi, F., Asheghian, L., and Kudva, J., "Design of a Flexible Skin for a Shear Morphing Wing," Journal of Intelligent Material Systems and Structures, Vol. 21 (17), November 2010, pp. 1755-1770, doi:10.1177/1045389X10382586.
14. Olympio, K. R., and Gandhi, F., "Optimal Cellular Core Topologies for One-Dimensional Morphing Aircraft Structures," J. Mech. Des., Aug. 2012, 134(8), 081005, http://dx.doi.org/10.1115/1.4007087.
15. Barbarino, S., Gandhi, F., and Webster, S., "Design of Extendable Chord Sections for Morphing Helicopter Rotor Blades," Journal of Intelligent Material Systems and Structures, Vol. 22 (9), June 2011, pp. 891-905, doi: 10.1177/1045389X11414077.
16. DiPalma, M. and Gandhi, F. "Optimizing Stiffness and Damping of Filled Cellular Lattice Structures using Response Surface Methods." *58th AIAA/ASCE/AHS/ASC Structures, Structural Dynamics, and Materials Conference*. Grapevine, Texas, Jan 9-13, 2017.

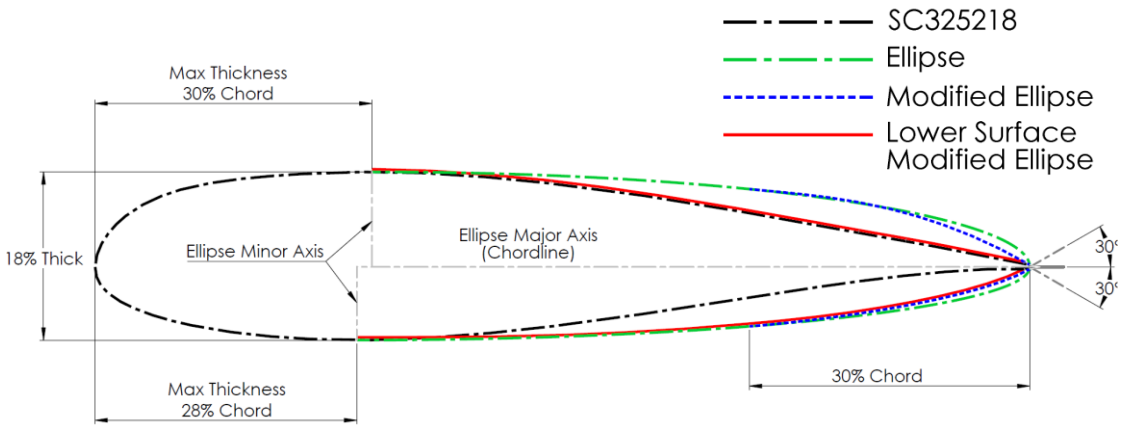

Figure 1. Baseline SC325218 airfoil and various morphed geometries considered for high-speed operation (red line for Lower Surface Modified Ellipse coincides with SC325218 on the top surface and Modified Ellipse on the bottom surface but is slightly offset for clarity)

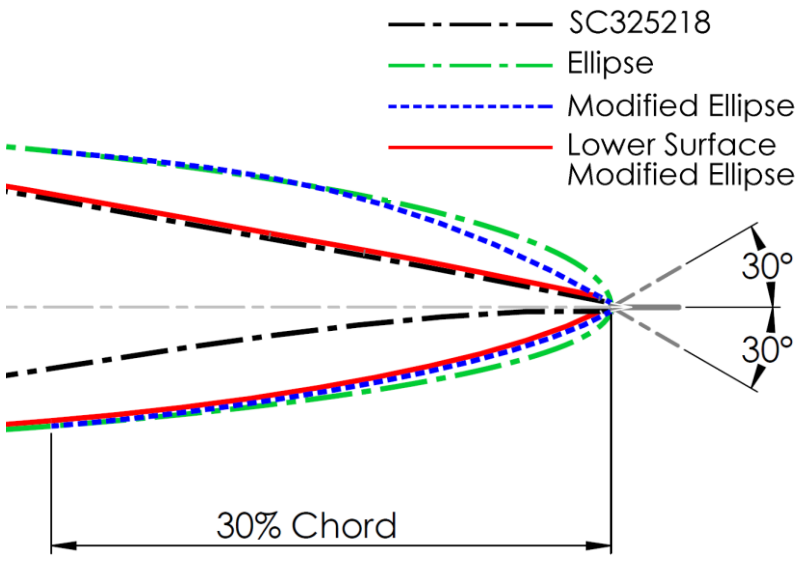

Figure 2. Close-up view of airfoil trailing edge region (red line for Lower Surface Modified Ellipse coincides with SC325218 on the top surface and Modified Ellipse on the bottom surface but is slightly offset for clarity)

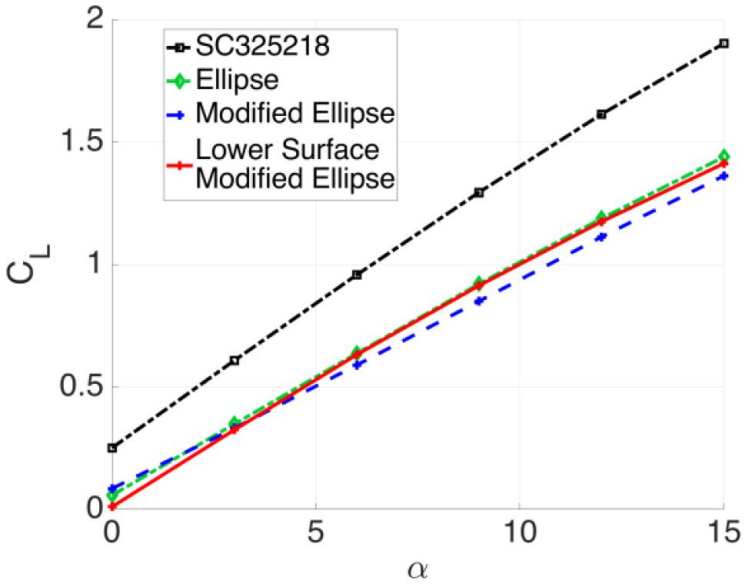

Figure 3: Airfoil lift coefficients in normal flow

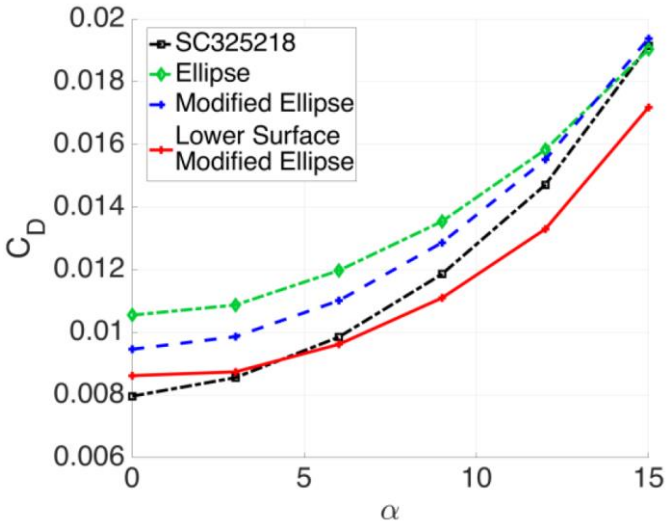

Figure 4: Airfoil drag coefficients in normal flow

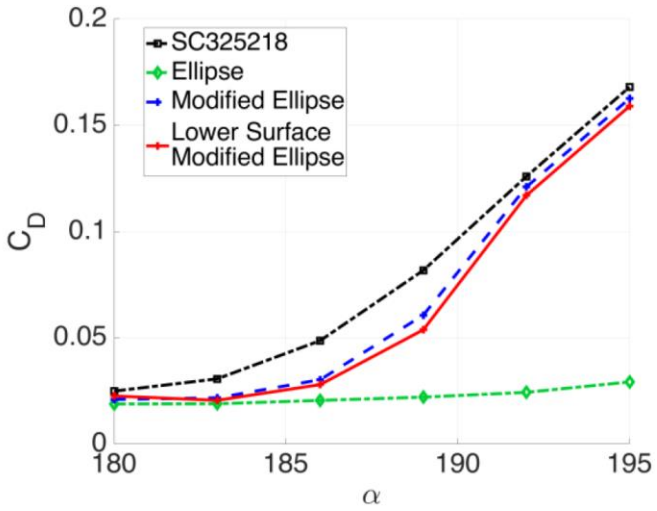

Figure 5: Airfoil drag coefficients in reverse flow

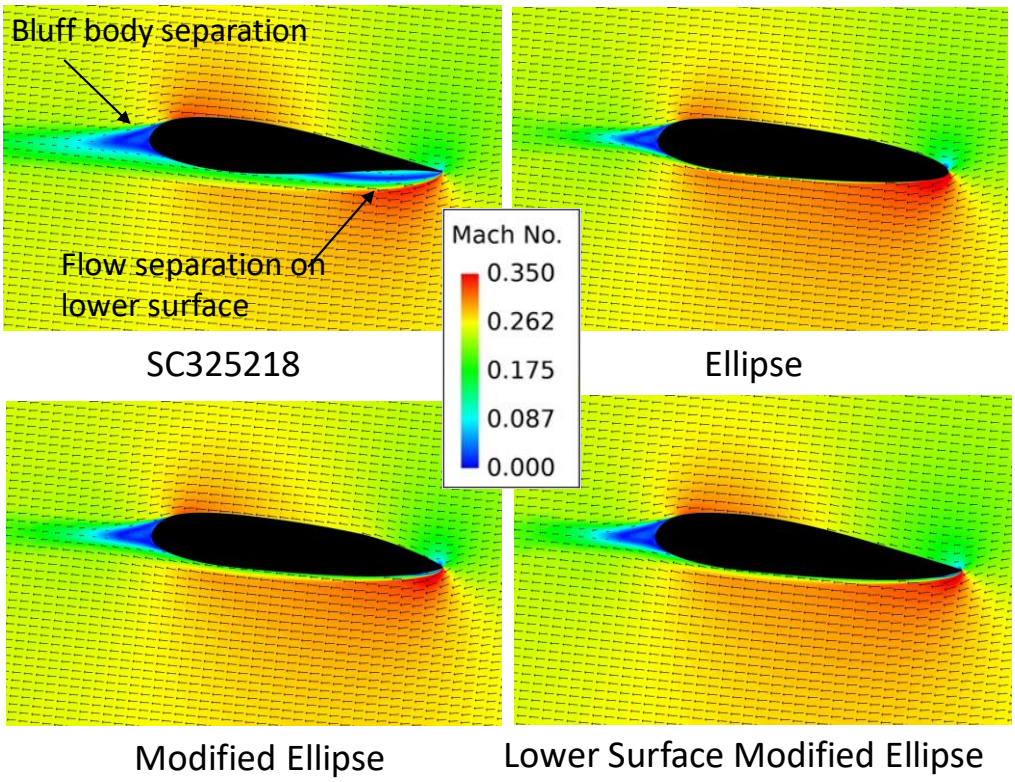

Figure 6. Flow field around various airfoils in reverse flow conditions

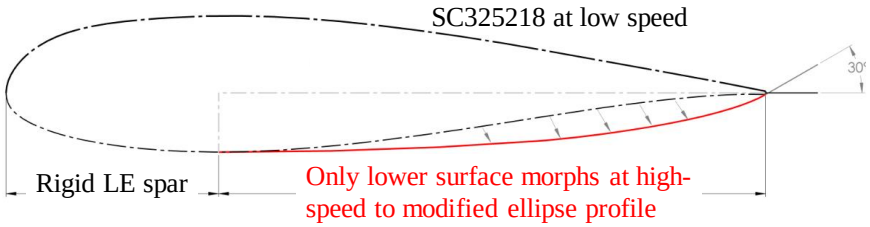

Figure 7: SC325218 for low speed, and lower surface morphing to modified ellipse (red) for high-speed operation

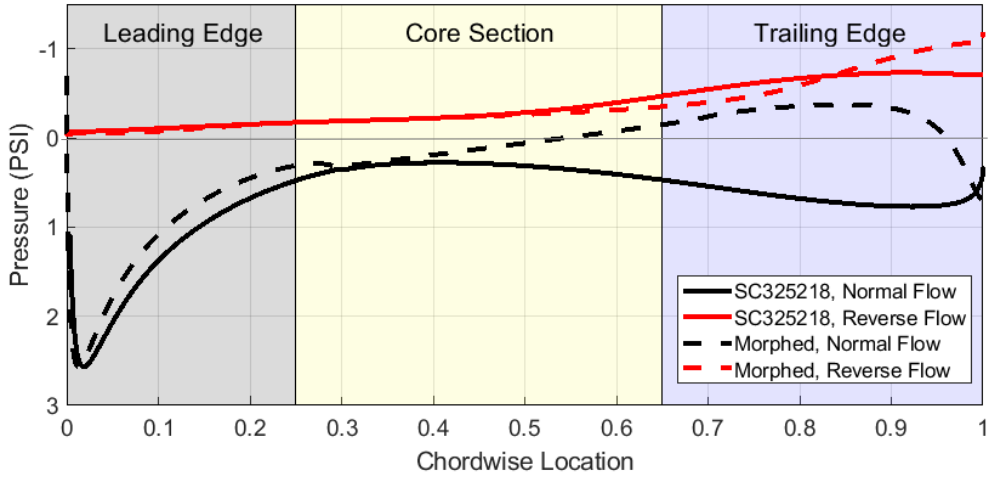

Figure 8: 4x lower surface aerodynamic pressure (at 9° angle of attack) in normal and reverse flow conditions

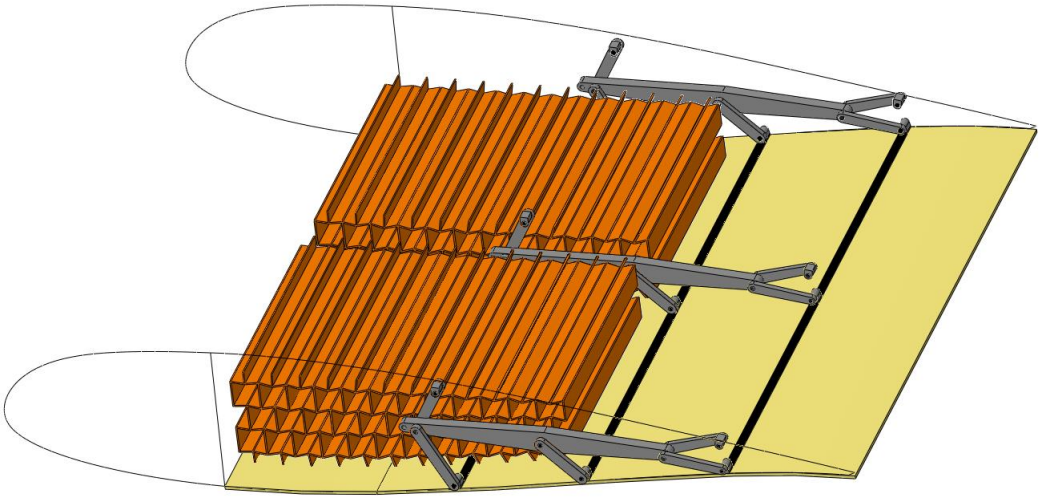

Figure 9a. Isometric system view

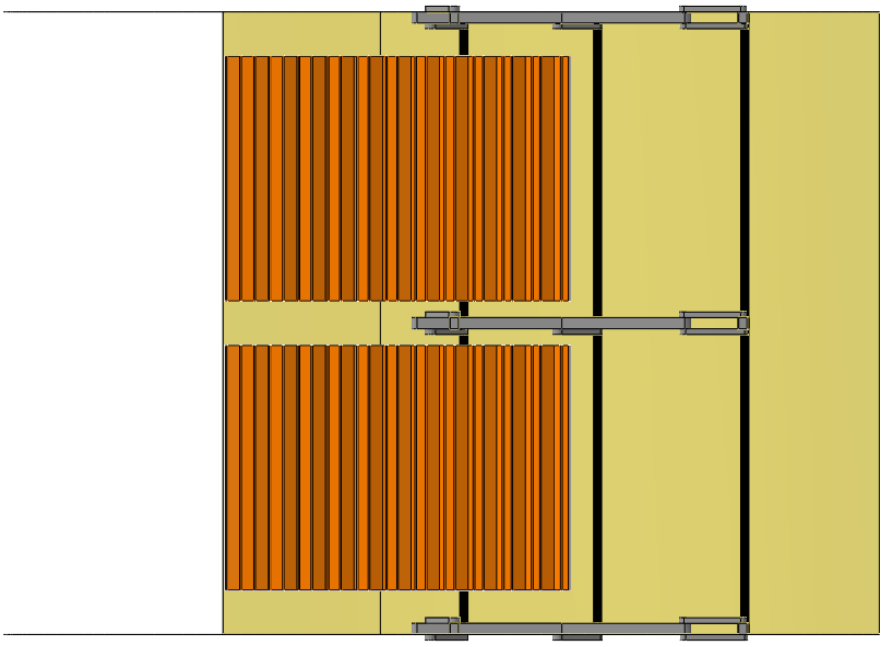

Figure 9b. Bird's eye system view

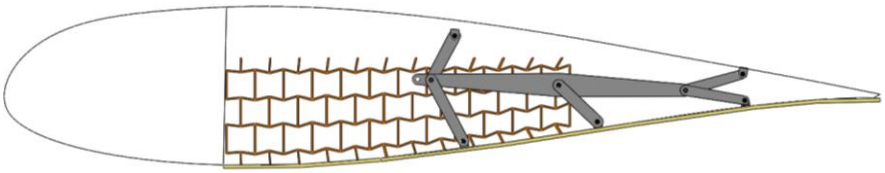

Figure 9c. Cross-sectional system view

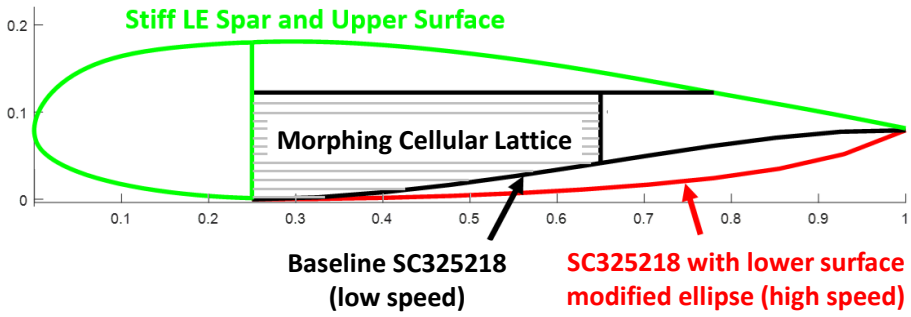

Figure 10: Morphing cellular lattice aft of spar (from 25% to 65% chord)

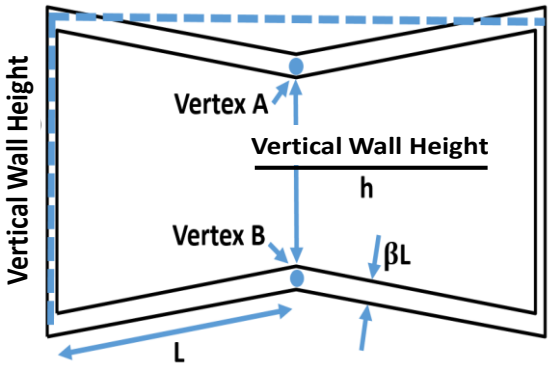

Figure 11: Morphing lattice unit cell, and cell parameters

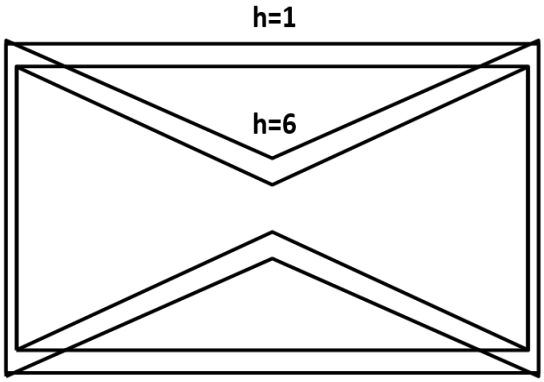

Figure 12: Cell hourglass ratio comparison

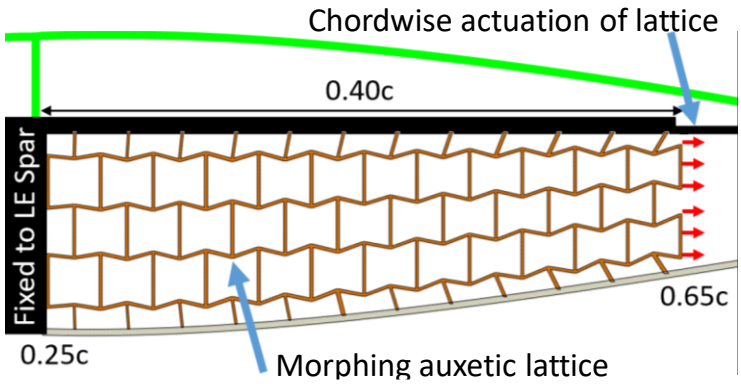

Figure 13: Auxetic lattice connection to LE spar, and to rigid upper support and lower skin by stumps

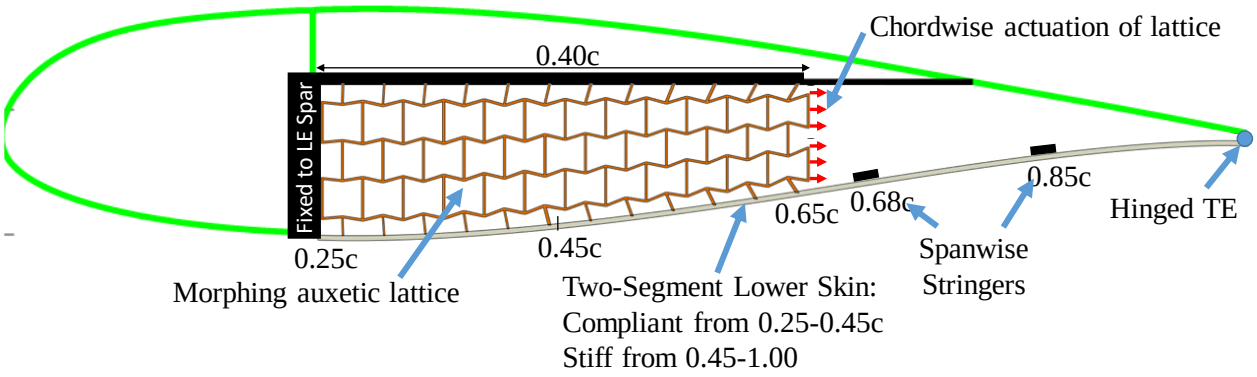

Figure 14: Full structural model

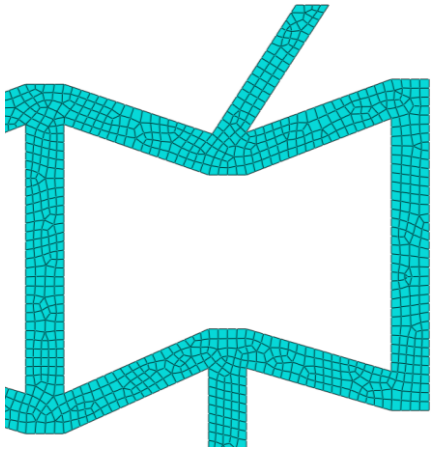

Figure 15. Finite element mesh for single lattice cell

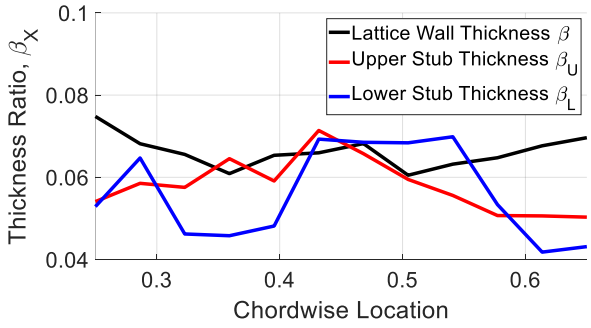

Figure 16a: Optimized wall thickness ratios

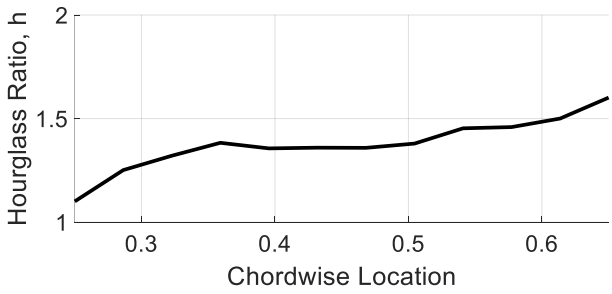

Figure 16b: Optimized hourglass ratio

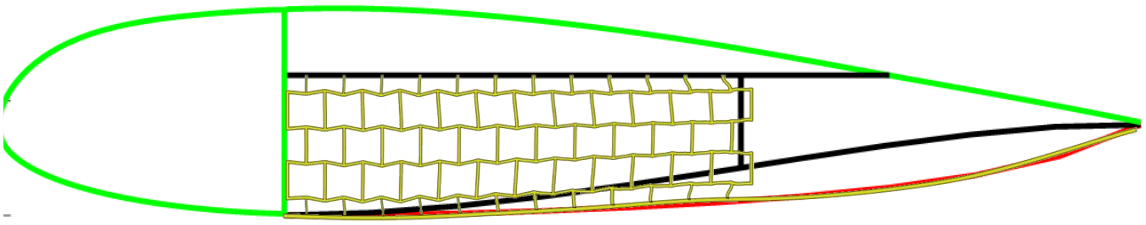

Figure 17: Optimized lattice in deformed configuration with lower surface matching target profile

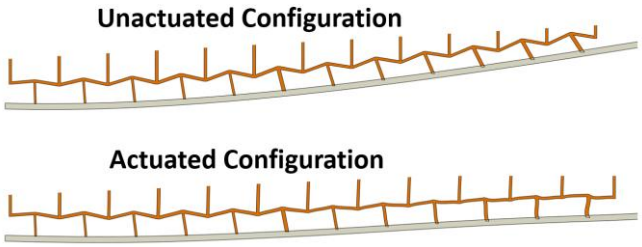

Figure 18: Lattice lower stumps in the unactuated and actuated configurations

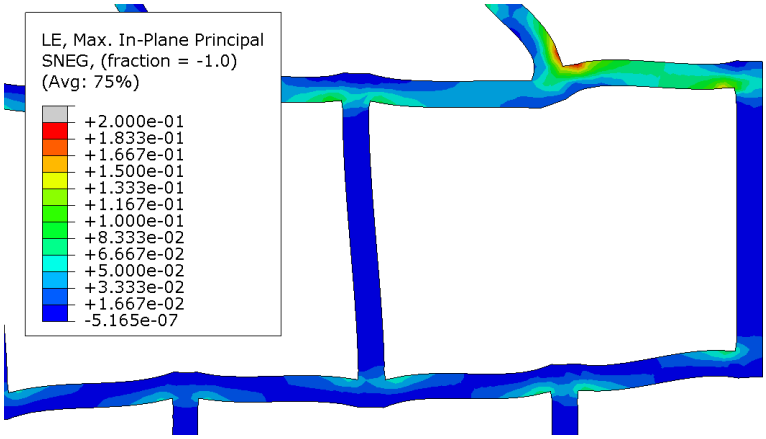

Figure 19: Peak strains in the auxetic lattice

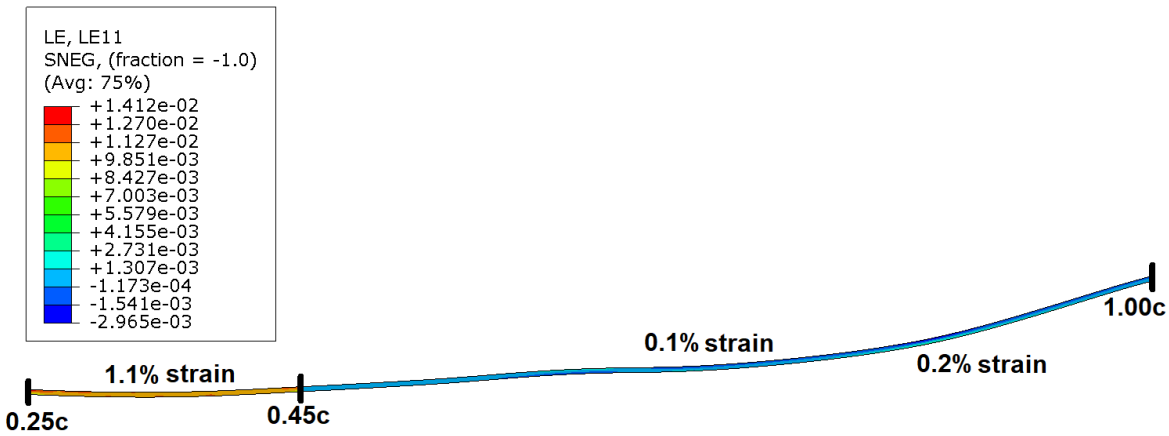

Figure 20: Lower skin strains in the deformed configuration

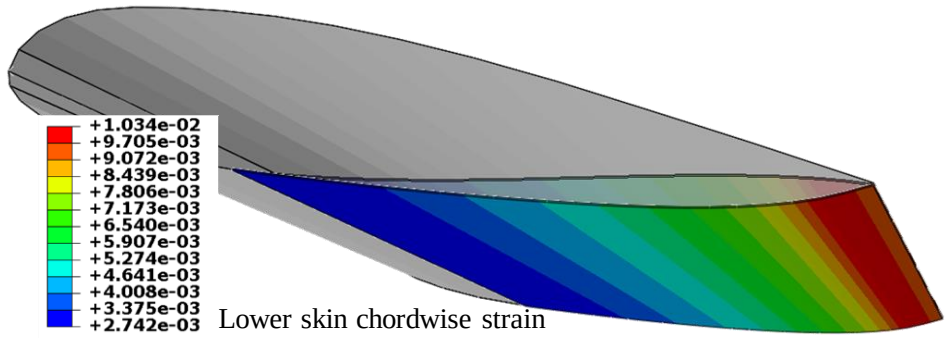

Figure 21: Skin strain associated with morphing from SC325218 to lower surface modified ellipse geometry

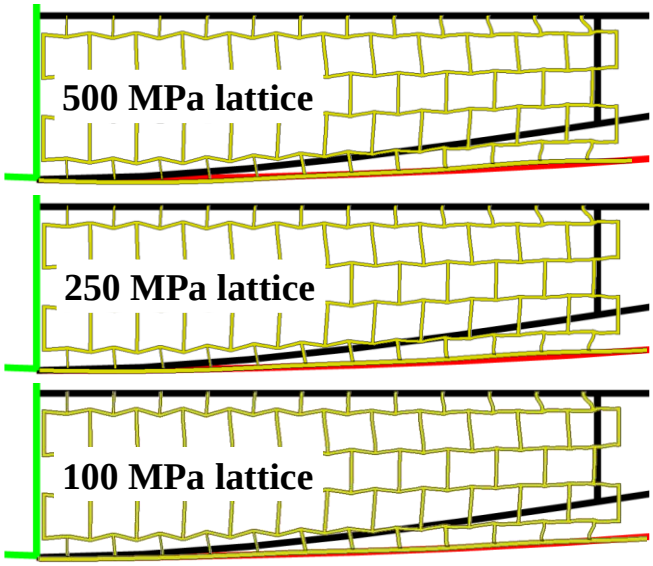

Figure 22: Comparison of lower skin profiles (yellow) under lattice actuation and reverse flow loading, for different values of lattice modulus (target profile in red)

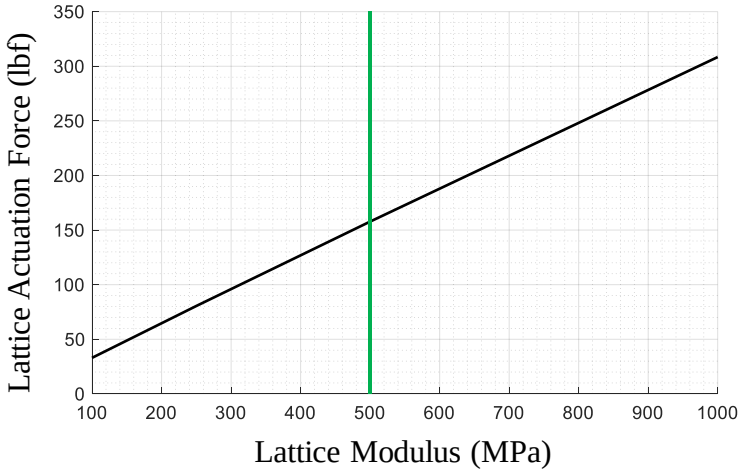

Figure 23: Lattice actuation force versus lattice modulus

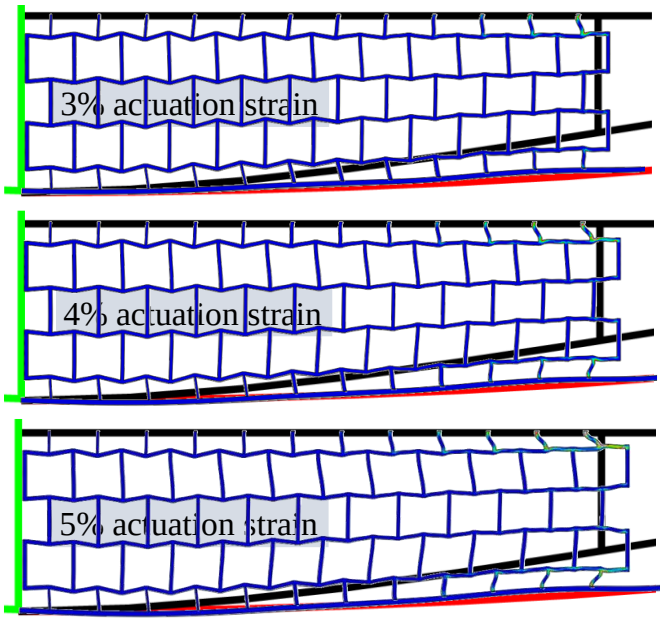

Figure 24: Morphed configuration for lattice actuation strains varying between 3% and 5% (target lower surface profile in red)

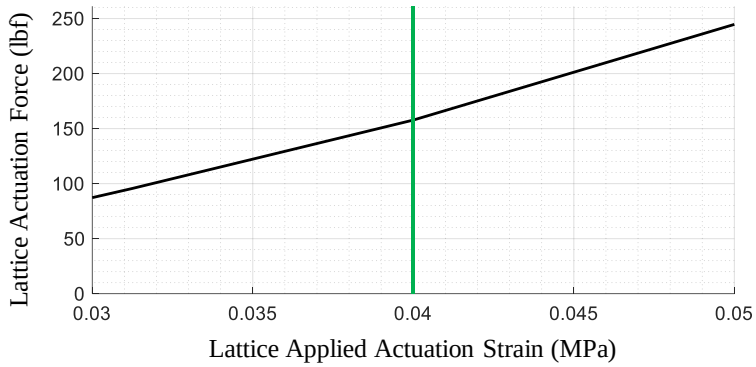

Figure 25: Lattice actuation force versus applied strain

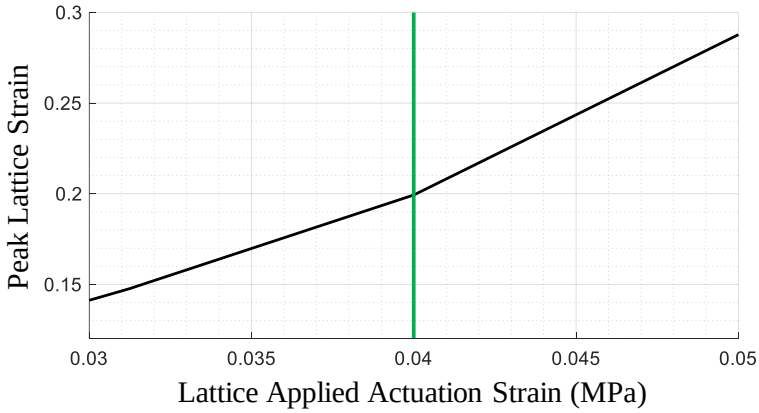

Figure 26: Peak lattice strain versus applied strain

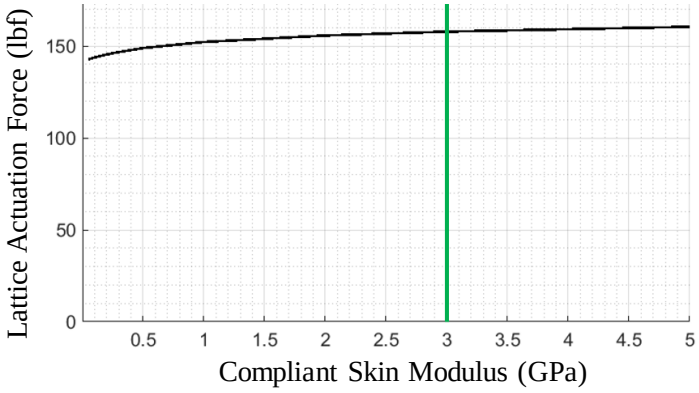

Figure 27: Lattice actuation force versus compliant skin modulus

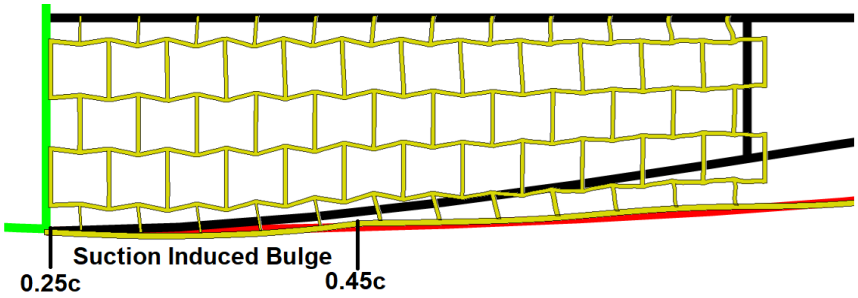

Figure 28: 100 MPa low modulus compliant skin deforming under reverse flow suction load (250 MPa lattice modulus, 3% applied strain)

APPENDIX

The ability of the cellular lattice to carry pressure loads in low-speed conditions (baseline SC325318 geometry) is examined here. The figures in the left column show that 500 MPa and 250 MPa lattices are effective in carrying the aerodynamic pressure (solid black line in Fig. 8 in the main body of the paper). Top right figure shows that further reducing lattice modulus 100 MPa results in cell wall buckling and lower surface deformation under aerodynamic loads. However, these three figures did not consider the presence of stringer support. Introducing spanwise stringers at 68% and 85% chord, even the 100 MPa lattice is able to carry the aerodynamic pressure loads (bottom right figure).